

# Journal of Biomedical Optics

[SPIEDigitalLibrary.org/jbo](http://SPIEDigitalLibrary.org/jbo)

## ***In vivo* photoacoustic imaging of mouse embryos**

Jan Laufer  
Francesca Norris  
Jon Cleary  
Edward Zhang  
Bradley Treeby  
Ben Cox  
Peter Johnson  
Pete Scambler  
Mark Lythgoe  
Paul Beard

# *In vivo* photoacoustic imaging of mouse embryos

Jan Laufer,<sup>a,b</sup> Francesca Norris,<sup>b</sup> Jon Cleary,<sup>a,b</sup> Edward Zhang,<sup>a</sup> Bradley Treeby,<sup>a\*</sup> Ben Cox,<sup>a</sup> Peter Johnson,<sup>b</sup> Pete Scambler,<sup>c</sup> Mark Lythgoe,<sup>b</sup> and Paul Beard<sup>a,b</sup>

<sup>a</sup>University College London, Department of Medical Physics and Bioengineering, Gower Street, London WC1E 6BT, United Kingdom

<sup>b</sup>University College London, Centre for Advanced Biomedical Imaging, Department of Medicine and Institute of Child Health, Paul O'Gorman Building, 72 Huntley Street, London WC1E 6DD, United Kingdom

<sup>c</sup>UCL Institute of Child Health, 30 Guilford Street, London WC1N 1EH, United Kingdom

**Abstract.** The ability to noninvasively image embryonic vascular anatomy in mouse models is an important requirement for characterizing the development of the normal cardiovascular system and malformations in the heart and vascular supply. Photoacoustic imaging, which can provide high resolution non invasive images of the vasculature based upon optical absorption by endogenous hemoglobin, is well suited to this application. In this study, photoacoustic images of mouse embryos were obtained *ex vivo* and *in vivo*. The images show intricate details of the embryonic vascular system to depths of up to 10 mm, which allowed whole embryos to be imaged *in situ*. To achieve this, an all-optical photoacoustic scanner and a novel time reversal image reconstruction algorithm, which provide deep tissue imaging capability while maintaining high spatial resolution and contrast were employed. This technology may find application as an imaging tool for preclinical embryo studies in developmental biology as well as more generally in preclinical and clinical medicine for studying pathologies characterized by changes in the vasculature. © 2012 Society of Photo-Optical Instrumentation Engineers (SPIE). [DOI: 10.1117/1.JBO.17.6.061220]

Keywords: photoacoustics imaging; embryo; *in vivo*.

Paper 11784 received Dec. 22, 2011; revised manuscript received Feb. 29, 2012; accepted for publication Mar. 7, 2012; published online May 18, 2012.

## 1 Introduction

The ability to characterize the structure and function of the embryonic vascular system in mouse models is an important requirement for a range of applications in developmental biological research. These include the study of the development of the normal cardiovascular system and the role of the blood supply in the development of organs, the musculoskeletal system and other anatomical structures. In addition, large-scale mutagenesis programmes are currently under way worldwide to create transgenic mouse models for each of the >25,000 genes in order to enable the study of gene function.<sup>1</sup> This increasing use of genetically modified mice has highlighted the need for techniques that can visualize abnormalities in cardiac and vascular development in genetically manipulated late-gestation embryos. Conventionally this is achieved *ex vivo* by microscopic examination with histology thus precluding performing longitudinal studies in the same animal.<sup>2</sup> As a consequence, there is a need for noninvasive imaging techniques that are capable of visualizing the evolution of embryonic vascular anatomy *in utero* (i.e., *in vivo* in the mother animal) over time, preferably without the use of exogenous contrast agents. The modalities that have shown the most promise for embryo imaging are ultrasound,<sup>3</sup> magnetic resonance imaging (MRI),<sup>4,5</sup> and x-ray computed tomography (CT).<sup>6</sup> However, in ultrasound imaging, which has been used to study early to mid-gestational embryos,<sup>3</sup> microbubble contrast agents are often required to overcome the low echogenicity of blood in

order to visualize the vasculature.<sup>3</sup> Although MRI has been used to visualise the heart and vasculature of the embryo *in vivo*,<sup>7</sup> it is more widely used in *ex vivo* studies,<sup>8</sup> due to the technical challenges of *in vivo* imaging. For example, the quality of *in vivo* embryo images is limited by motion artefacts and poor spatial resolution due to the limited image acquisition time available. X-ray CT provides weak, soft tissue contrast and typically requires the use of exogenous contrast agents to visualize the vasculature. In addition, the use of ionizing radiation can limit the duration of longitudinal studies.

Photoacoustic imaging is an emerging technique that can provide label-free noninvasive three-dimensional images of the vasculature<sup>9</sup> to depths of several cm with a spatial resolution ranging from tens to hundreds of microns (depending on depth). It is based upon the generation of ultrasound waves through the absorption of nanosecond laser pulses by light absorbing tissue chromophores. The acoustic waves travel to the tissue surface where they are detected by an ultrasound receiver array. From the detected signals, three-dimensional (3-D) images that are proportional to the absorbed optical energy distribution can be reconstructed. The fundamental advantage of photoacoustic imaging is that it combines the physics of both optical and ultrasound imaging thus providing both the spectral specificity of purely optical methods and the high spatial resolution of ultrasound. Image contrast is dominated by optical absorption making the technique well suited to visualizing the vasculature due to the strong absorption exhibited by hemoglobin at visible and nearinfrared wavelengths. As well as providing images of vascular anatomy, quantitative spectroscopic measurements of blood oxygen saturation and hemoglobin concentration<sup>10</sup> can be made by acquiring images at multiple wavelengths. In addition, there is the potential for measuring blood flow using

\*Bradley Treeby is currently at Australian National University, Research School of Engineering, College of Engineering and Computer Science, Building 115, North Road, Canberra ACT 0200, Australia.

Address all correspondence to: Jan Laufer, Julius Wolff Institut, Charité – Universitätsmedizin Berlin, Berlin 13353, Germany. Tel: +49 30 450 539 419; Fax: +49 30 450 539 918; E-mail: [jan.laufer@charite.de](mailto:jan.laufer@charite.de)

Doppler techniques.<sup>11–13</sup> These attributes suggests photoacoustic imaging has strong potential as a preclinical investigative tool for the noninvasive assessment of embryonic vascular structure and function.

Photoacoustic imaging has been used previously to obtain noninvasive tomographic images of the vasculature of major organs in mice, such as the brain<sup>14</sup> and the skin.<sup>15</sup> The potential of photoacoustic imaging to visualize the vascular anatomy of mouse embryos *ex vivo* has been demonstrated in preliminary studies<sup>16,17</sup> but not *in situ* or *in vivo*. In this paper, we demonstrate for the first time deep tissue (>10 mm) 3-D imaging of whole mouse embryos *in vivo* (and *in utero*) using an all-optical PA scanner and an image reconstruction algorithm based on acoustic time reversal.

## 2 Methods

### 2.1 Photoacoustic Imaging System

An all-optical photoacoustic imaging system was used to image mouse embryos in tomography mode. The system, a schematic and photograph of which is shown in Fig. 1, is described in detail elsewhere.<sup>18</sup> Briefly, it comprises a wavelength tuneable optical parametric oscillator (OPO) laser system (premiScan, GWU, and Quanta-Ray PRO-270-50, Newport Spectra-Physics) that provides visible and near infrared nanosecond excitation laser pulses and a photoacoustic scanner based on a planar Fabry-Perot ultrasound sensor for mapping the photoacoustic waves. The sensor consists of two dichroic mirrors separated by a polymer film, thus forming a Fabry-Perot interferometer (FPI). The mirrors have high transmittance between 590 and 1200 nm but are highly reflective around 1550 nm. This allows the excitation laser pulses to be transmitted through the Fabry-Perot sensor into the adjacent tissue where they are absorbed by chromophores such as oxy- and deoxyhemoglobin. The absorption produces a rapid isochoric increase in temperature and pressure. The latter subsequently relaxes resulting in the emission of broadband ultrasonic waves. As the waves propagate through

the sensor, the optical thickness of the FPI is modulated, causing a transient change in its reflectivity. By raster scanning a focussed 1550 nm continuous-wave (CW) laser beam across the surface of the FPI and recording the time-varying reflected intensity at each point, the spatial-temporal distribution of the incident photoacoustic waves can be mapped in 2-D.

In this study, a Fabry-Perot sensor of 40  $\mu\text{m}$  thickness was used, which provides a detection bandwidth of 22 MHz ( $-3$  dB point). The line spread function (LSF) represents the inherent instrument-limited spatial resolution in the absence of tissue acoustic attenuation. The vertical LSF is limited by the detector bandwidth and is 27  $\mu\text{m}$ . The lateral LSF is determined by several parameters, such as the step size, scan area aperture, and bandwidth.<sup>18</sup> In this study, it is defined by the relatively large scan step size, which ranged from 115 to 150  $\mu\text{m}$ . The noise equivalent pressure of the sensor was 0.21 kPa over a measurement bandwidth of 20 MHz. The diameter of the focused interrogation laser beam was 22  $\mu\text{m}$  which, to a first approximation, defines the acoustic element size. The maximum scan area was  $16 \times 16 \text{ mm}^2$ . A typical scan acquired 20,000 waveforms each of 500 points without signal averaging. The image acquisition time was typically 8 min and limited by the 50 Hz pulse repetition frequency of the excitation laser. All images were acquired using fluences below the maximum permissible exposure for skin.<sup>19</sup>

### 2.2 Time-Reversal Image Reconstruction

Photoacoustic images were reconstructed from the detected photoacoustic signal using a time-reversal image reconstruction algorithm, which compensates for the frequency dependent acoustic attenuation exhibited by soft tissues.<sup>20</sup> The algorithm uses a pseudo-spectral ( $k$ -space) acoustic propagation model<sup>21</sup> to simulate the retransmission of the measured photoacoustic signals into the domain in time-reversed order. The photoacoustic waves then refocus to yield an image of the initial pressure distribution. Attenuation compensation is provided

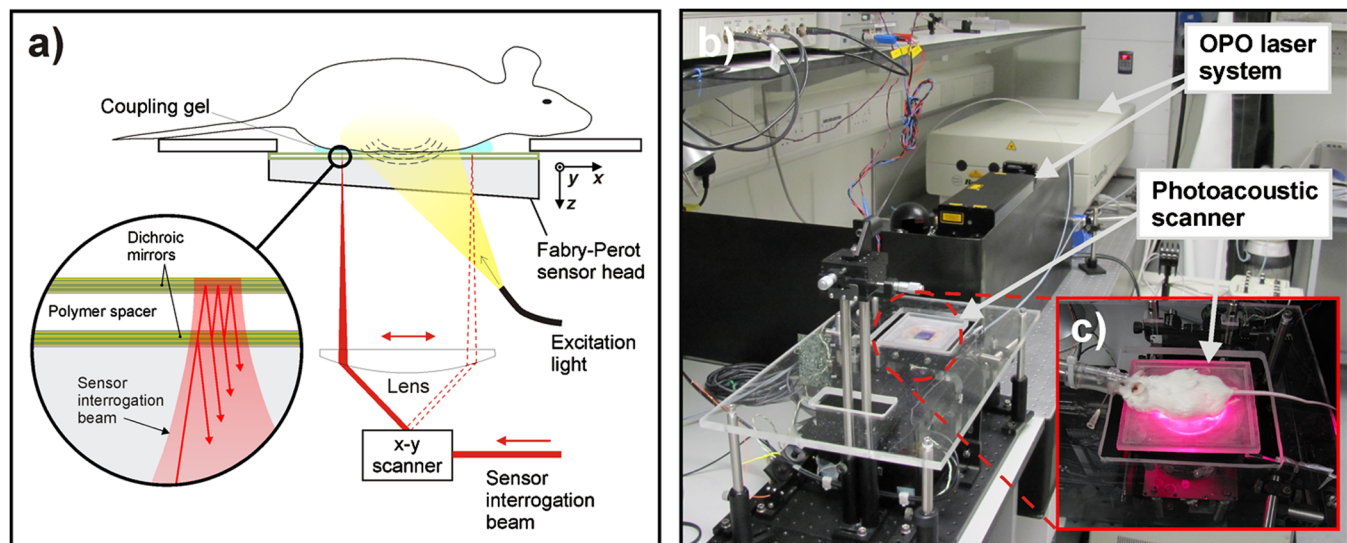


**Fig. 1** Small animal photoacoustic imaging system. (a) Schematic illustrating the operation of the system. Photoacoustic waves are generated by the absorption of nanosecond optical pulses provided by a wavelength-tuneable OPO laser and detected by a transparent Fabry-Perot polymer film ultrasound sensor. The sensor comprises a pair of dichroic mirrors separated by a 40  $\mu\text{m}$  thick polymer spacer thus forming a Fabry-Perot interferometer (FPI). The waves are mapped in 2-D by raster-scanning a CW focused interrogation laser beam across the sensor and recording the acoustically induced modulation of the reflectivity of the FPI at each scan point. (b) Photograph of the imaging system. (c) The system in operation, showing the anesthetized animal located on the Fabry-Perot sensor, through which the excitation laser pulses are transmitted.

via an acoustic equation of state which accounts for acoustic absorption following a frequency power law. This significantly increases image magnitude and resolution, especially at greater depths.<sup>20</sup> The attenuation parameters were set to those of human breast tissue<sup>22</sup> with an absorption coefficient  $\alpha = \alpha_0 f^y$  dB cm<sup>-1</sup> where  $f$  is the frequency,  $\alpha_0 = 0.75$  dB MHz<sup>-y</sup> cm<sup>-1</sup> and  $y = 1.5$ . The sound speed was determined using an autofocus method.<sup>23</sup> This involved using a fast FFT-based reconstruction algorithm<sup>24</sup> without attenuation compensation to reconstruct a number of images using different sound speeds. A metric related to image sharpness was calculated for each image, and the sound speed corresponding to its maximum was chosen for the final image reconstruction using the time reversal algorithm.

For display purposes, the reconstructed 3-D images were interpolated onto a mesh with four times higher grid density in  $x$  and  $y$ . To aid visualization of deeper lying features, the image intensity was normalized with respect to depth using a one-dimensional exponential function to account for optical attenuation. Maximum intensity projections (MIP) were computed from the 3-D image data set and displayed using a logarithmic image intensity scale. Three dimensional rendering was accomplished using 3-D-Doctor (Able Software Corp.).

### 2.3 Embryo Imaging

Three sets of experiments were performed. In the first set, embryos of CD-1 mice at two stages of development (E15.5 and E18.5, i.e., 15.5 days and 18.5 days gestation) were imaged *ex vivo* within 1 h of dissection. The embryos were placed on the

scanner and immersed in a strongly scattering intralipid suspension (Fresenius Kabi) of 1% lipid concentration in order to homogenize the incident illumination. The embryos were irradiated either through the sensor (backward mode) or from above (forward mode) or in both forward and backward modes simultaneously using the signal and idler outputs of the OPO laser system.

The second set of experiments was aimed at demonstrating the feasibility of imaging embryos *in situ* and involved imaging the abdomen of two pregnant CD-1 mice (E15.5) within 1 h of sacrifice. The fur on the abdomen was removed using commercial hair removal products. The skin remained intact. The abdomen of the animals was then placed on the Fabry-Perot sensor with a thin layer of aqueous gel inserted between the skin and the sensor to provide acoustic coupling. The abdomen was illuminated through the sensor (backward mode).

The third set of experiments was aimed at establishing the feasibility of *in vivo* imaging of mouse embryos in the mother animal. A pregnant CD-1 mouse (E15.5) was anesthetized using a mixture of oxygen and isoflurane at a concentration of 4% for induction and 1% to 2% for maintenance. The flow rate was 1.1 min<sup>-1</sup>. Body temperature and respiration were monitored and maintained constantly during the experiment.

For all experiments, the beam diameter of the incident excitation light was approximately 2 cm. This resulted in a fluence of <10 mJ cm<sup>-2</sup>, which is below the maximum permissible exposure for skin.<sup>19</sup> The excitation wavelengths ranged from 600 to 770 nm and the duration of the scans was approximately 8 min.

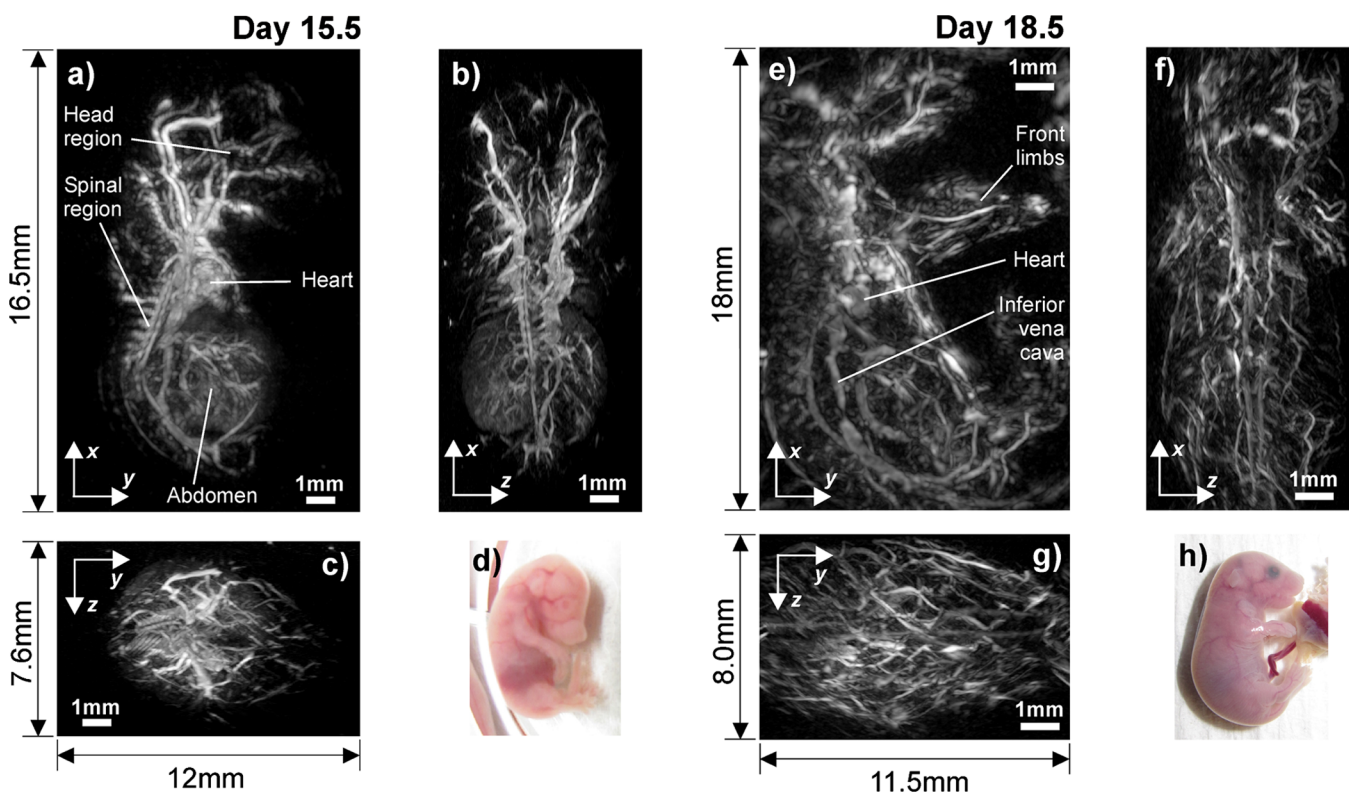


**Fig. 2** *Ex vivo* photoacoustic images of two mouse embryos of different age. (a)  $x - y$ , (b)  $x - z$ , and (c)  $y - z$  maximum intensity projections (MIP) of a 3-D image data set acquired in an E15.5 embryo using 658 and 770 nm excitation wavelengths simultaneously (d) photograph of embryo. (e)  $x - y$ , (f)  $x - z$ , and (g)  $y - z$  MIPs of an E18.5 embryo obtained using an excitation wavelength of 630 nm (h) photograph of embryo. The scan step size for both data sets was 120  $\mu$ m. Movies of volume rendered 3-D representations of both data sets are available online (Video 1, MOV, 3.9 MB). [URL: <http://dx.doi.org/10.1117/1.JBO.17.6.061220.1>] (Video 2, MOV, 4.0 MB). [URL: <http://dx.doi.org/10.1117/1.JBO.17.6.061220.2>].

### 3 Results

#### 3.1 *Ex Vivo* Photoacoustic Images of Mouse Embryos

Figure 2 shows *ex vivo* images of two embryos at different stages of development. To obtain these images, forward and backward mode illumination were used simultaneously. Figure 2(a)–2(c) shows MIPs ( $16.5 \times 12.0 \times 7.6 \text{ mm}^3$ ) of the 3-D image data set of an E15.5 embryo. Figure 2(a) shows regions such as the head, heart, abdomen and spine. Figure 2(e)–2(g) shows MIPs ( $18.0 \times 11.5 \times 8.0 \text{ mm}^3$ ) of an E18.5 embryo and illustrates the more advanced anatomical development. 3-D volume rendered representations of the

image data sets shown in Fig. 2 can be viewed online in Videos 1 and 2.

A more detailed visualization of the vasculature in the interior of the smaller E15.5 embryo is provided in Fig. 3 which shows a set of MIP slices at different depths through the embryo. Figure 3(a) shows the  $x-y$  MIP of the entire 3-D image data set of the embryo (also available online as a flythrough movie, Video 3). Figure 3(b)–3(f) shows MIPs of this data set for different depth ranges. Figure 3(b) shows that the vertebral and right pulmonary arteries, the superficial temporal vein, and liver tissue can be readily visualized. Unexpectedly, the developing ribs can also be seen. This is typically not the case

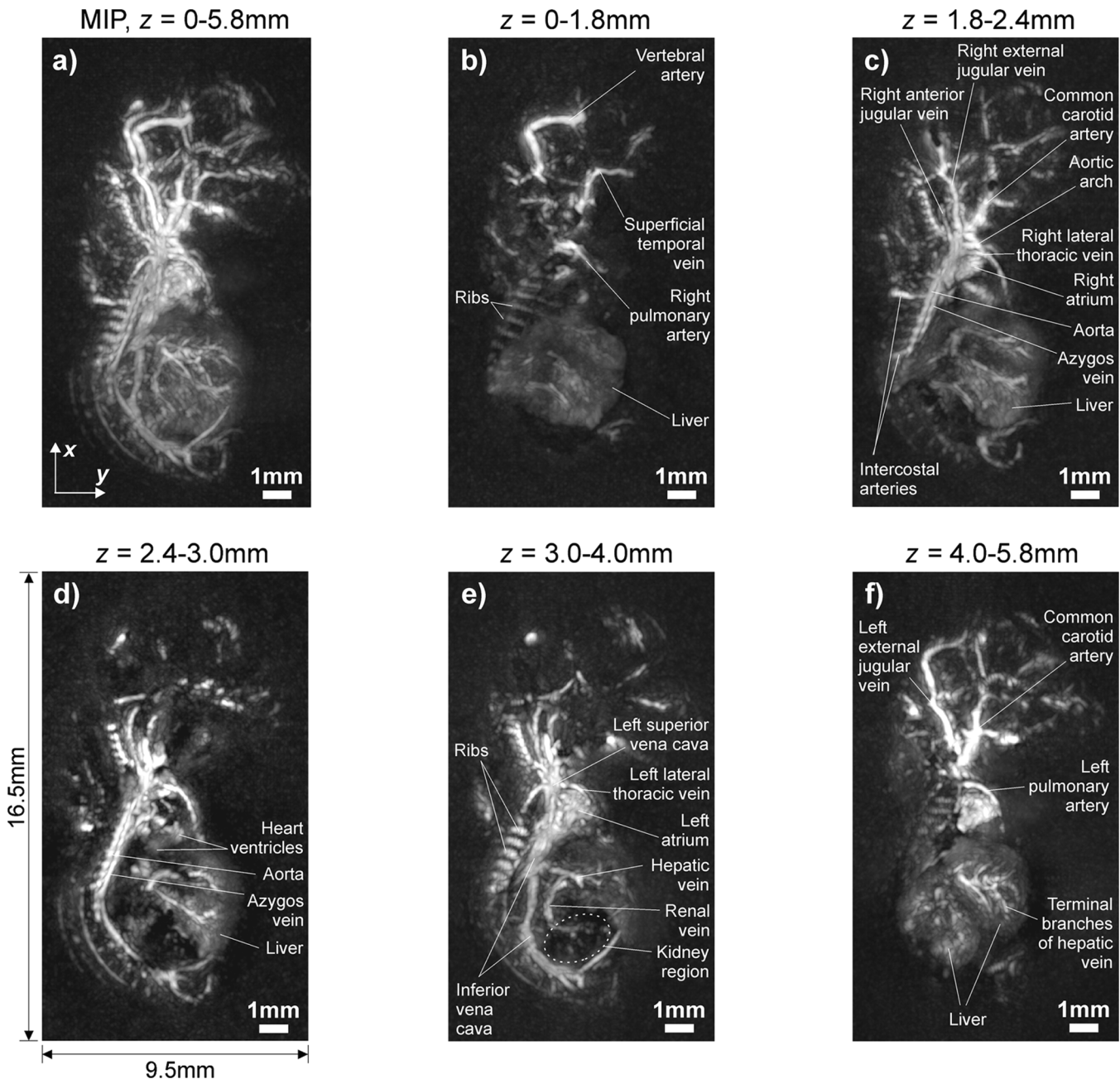


**Fig. 3**  $x-y$  MIP photoacoustic images of the E15.5 embryo shown in Fig. 2(d) for different depth ranges. (a) complete *ex vivo* 3-D image data set [ $z = 0$  to  $5.8 \text{ mm}$ , same image as Fig. 2(a)]. (b)  $z = 0$  to  $1.8 \text{ mm}$ , (c)  $z = 1.8$  to  $2.4 \text{ mm}$ , (d)  $z = 2.4$  to  $3.0 \text{ mm}$ , (e)  $z = 3.0$  to  $4.0 \text{ mm}$ , (f)  $z = 4.0$  to  $5.8 \text{ mm}$ . A flythrough movie of this image data set is available online (Video 3, MOV, 4.9 MB). [URL: <http://dx.doi.org/10.1117/1.JBO.17.6.061220.3>].

in adult mice, as bone tissue has limited photoacoustic contrast due to its low hemoglobin content. Figure 3(c) shows the vasculature around the right atrium of the heart, such as the lateral thoracic vein, the aorta and the aortic arch, Azygos vein, and the jugular vein. The intercostal arteries, which branch off the aorta towards the region of the developing spine, can also be seen. Figure 3(d) shows the MIP for  $z = 2.4$  to  $3.0$  mm and reveals features resembling the heart ventricles. The lower image contrast produced by the ventricles compared to that of the heart atria may be a consequence of differences in their

anatomical structure. While the atria are smooth walled compartments at this stage of embryonic development, the developing ventricles are trabeculated structures,<sup>25</sup> which may hold less blood volume than the atria and therefore produce less photoacoustic contrast. Figure 3(e) shows sections of the heart, such as the left atrium, and major parts of the vasculature, such as the left lateral thoracic vein and the left superior vena cava. The most noticeable feature is the inferior vena cava and its branches, such as the hepatic and renal veins. Also, regions corresponding to the developing bone tissue, such as the ribs, are again clearly

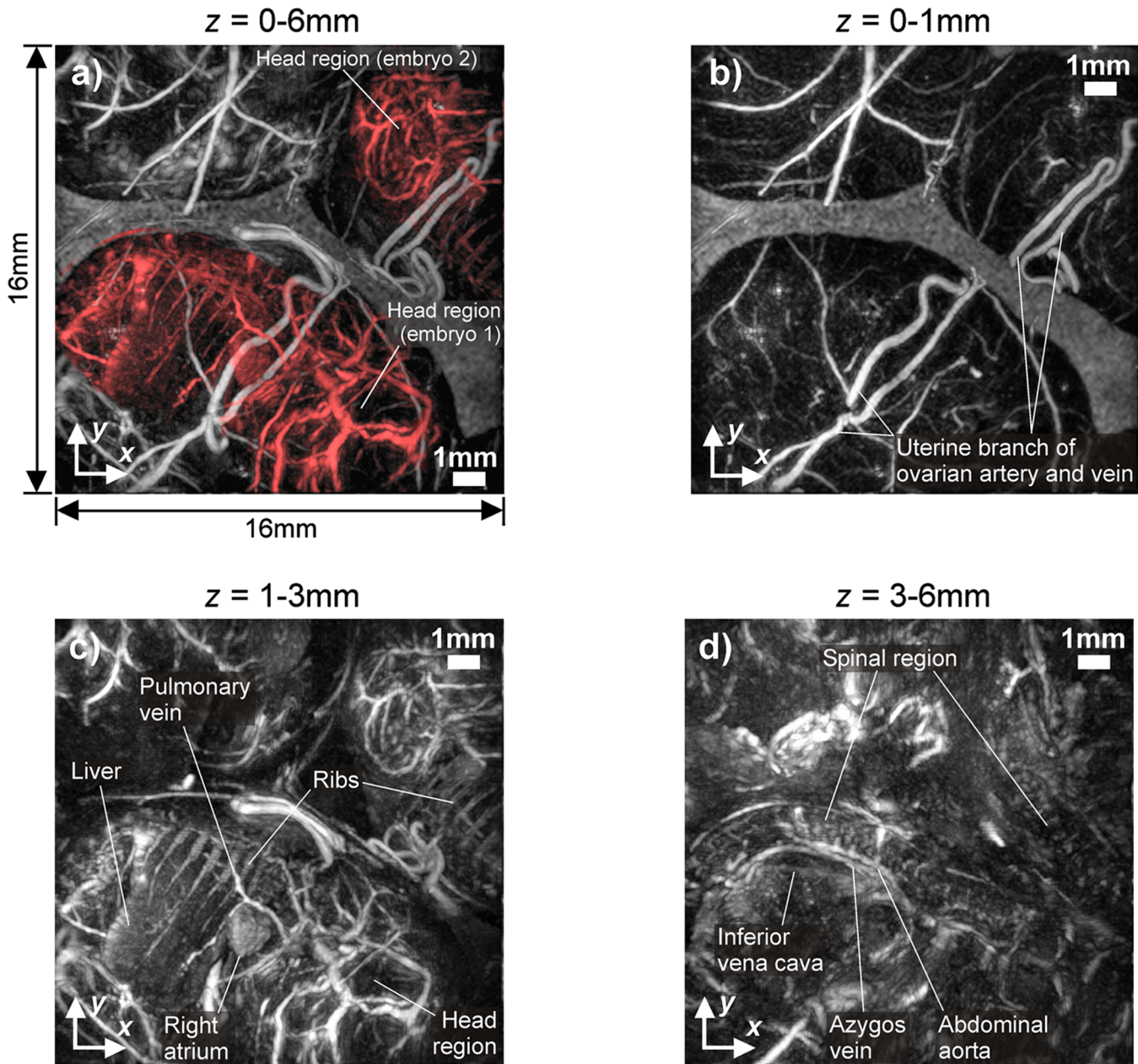


**Fig. 4** *In situ* images of the abdomen of a pregnant female mouse containing two embryos for different depth ranges. The excitation wavelength was 640 nm and the step size was  $115 \mu\text{m}$ . (a)  $x - y$  MIP of complete 3-D image data set ( $z = 0$  to  $6$  mm) showing the two embryos (shaded red), (b)  $x - y$  MIP for  $z = 0$  to  $1$  mm showing the blood vessel network in the abdominal skin and the uterus. (c)  $x - y$  MIP for  $z = 1$  to  $3$  mm. This shows the anatomy of the two embryos. The right atrium, the pulmonary vein, and the vessels in the embryo head are evident as are organs such as the liver and parts of the developing skeleton, such as the ribs. (d)  $x - y$  MIP for  $z = 3$  to  $6$  mm showing vascular features such as the abdominal aorta, the Azygos vein, and the inferior vena cava. The spinal region, which contains the intercostal arteries, is also visible. A flythrough movie of this image is available online (Video 4, MOV, 6.8 MB). [URL: <http://dx.doi.org/10.1117/1.JBO.17.6.061220.4>].

evident. Figure 3(f) shows major external blood vessels, such as the left external jugular vein, and internal vessels, such as the common carotid, the left pulmonary artery, and the terminal branches of the hepatic vein within the liver.

### 3.2 *In Situ* Embryo Images

Images of the abdomen of a pregnant female mouse containing two embryos (acquired within 1 h of sacrifice) are shown in Fig. 4. In Fig. 4(a), the  $x-y$  MIP of the entire 3-D image data set for  $z = 0$  to 6 mm is presented—a flythrough movie of this image data set is available in Video 4. Two embryos (shaded red) can be seen in Fig. 4(a), along with the vasculature of the uterus and the skin. In order to distinguish between the maternal and embryonic anatomy, MIPs over different depth ranges are shown in Fig. 4(b)–4(d). Figure 4(b) shows the  $x-y$  MIP for  $z = 0$  to 1 mm and reveals the maternal blood vessel network in the abdominal skin and the uterus, including branches of the ovarian arteries and veins. Since most of the embryonic vascular anatomy is located beyond the depth range of this image, the embryos themselves are barely visible. By contrast, both embryos can be clearly seen in Fig. 4(c) which is an MIP over the depth range  $z = 1$  to 3 mm. The pulmonary vein, the right atrium of the heart and the liver of embryo 1 are evident as are the blood vessels in the head and parts of the developing skeleton (such as the ribs) of both embryos. Figure 4(d) shows the abdominal aorta and the Azygos vein, which are two major blood vessels that run along the abdominal side of the spine, and the inferior vena cava of embryo 1. The spinal region, which contains the intercostal arteries branching off the abdominal aorta, of both embryos is also visible. Figure 5 shows an  $x-y$  MIP

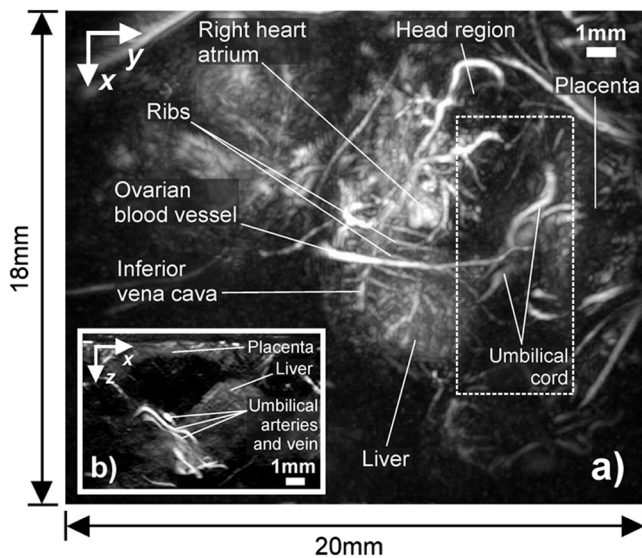


**Fig. 5**  $x-y$  MIP of a 3-D image data set ( $z = 0$  to 6.5 mm) of the abdomen of a pregnant mouse acquired *in situ* at an excitation wavelength of 640 nm and a step size of 140  $\mu\text{m}$ , showing the placenta and umbilical cord as well as the vasculature of the embryo (heart, liver, and head), the developing rib cage, and the ovarian blood vessels. A flythrough movie of this 3-D image can also be viewed online (Video 5, MOV, 2.55 MB). [URL: <http://dx.doi.org/10.1117/1.JBO.17.6.061220.5>]. (b)  $x-z$  MIP of an image subsection (as indicated by the dashed rectangle in the  $x-y$  image) with a thickness of 4 mm in the  $y$ -direction. Three blood vessels of the umbilical cord, i.e., two arteries and one vein, can be seen.

( $z = 0$  to 6.5 mm) of the abdomen of a different pregnant mouse. In this example, only a single embryo can be seen. In addition to the embryonic anatomical features observed in Fig. 4, the placenta and umbilical cord are also visible—the visualization of these features is relevant to the study of the interplay between the morphology of the maternal feeding vessels and embryonic development and abnormalities. A fly-through movie of this image is available in Video 5.

### 3.3 *In Vivo* Mouse Embryo Images

Figure 6 shows an MIP of a 3-D *in vivo* image of the abdomen of a pregnant mouse (E15.5). The embryo is highlighted in red. The maternal vasculature in the abdominal skin is clearly evident as well as considerable photoacoustic contrast originating from the gastrointestinal tract, most likely the bowel. To visualize the embryo more clearly,  $x-y$  MIPs of a smaller subsection ( $12 \times 12 \times 10 \text{ mm}^3$ ) of the data set are shown in Fig. 7 for six different depth ranges. The vasculature of the abdominal skin and the uterus can be seen in Fig. 7(a), which shows the  $x-y$  MIP of the reduced data set for  $z = 0$  to 1.2 mm. It also shows a small section of the gastrointestinal tract. Figure 7(b) shows the MIP for  $z = 1.2$  to 1.8 mm in which the superficial vasculature of the embryo and the walls of the oval-shaped uterus can be seen. Figure 7(c) shows the MIP for  $z = 1.8$  to 3.7 mm. Sections of the interior anatomy of the embryo, such as the left heart atrium, the superior vena cava and the exterior vasculature, such as the pulmonary vein and the anterior facial vein, are visualized. The liver can also be seen. At depths greater than 4 mm, the resolution is noticeably reduced compared to the *in situ* images (Fig. 4), which is most likely due to respiratory movement. Major blood vessels can nevertheless be identified.

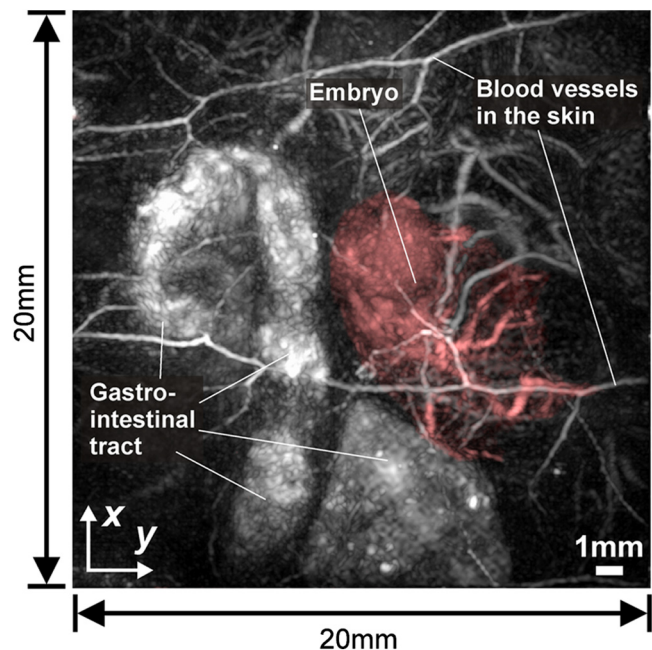


**Fig. 6** *In vivo*  $x-y$  MIP of a 3-D image data set ( $20 \times 20 \times 10 \text{ mm}^3$ ) of the abdomen of a pregnant mouse (E15.5) containing a single embryo acquired using an excitation wavelength of 640 nm and a scan step size of 150  $\mu\text{m}$ . It shows the maternal skin vasculature, parts of the gastrointestinal tract, and the location of the embryo, which is indicated in red.

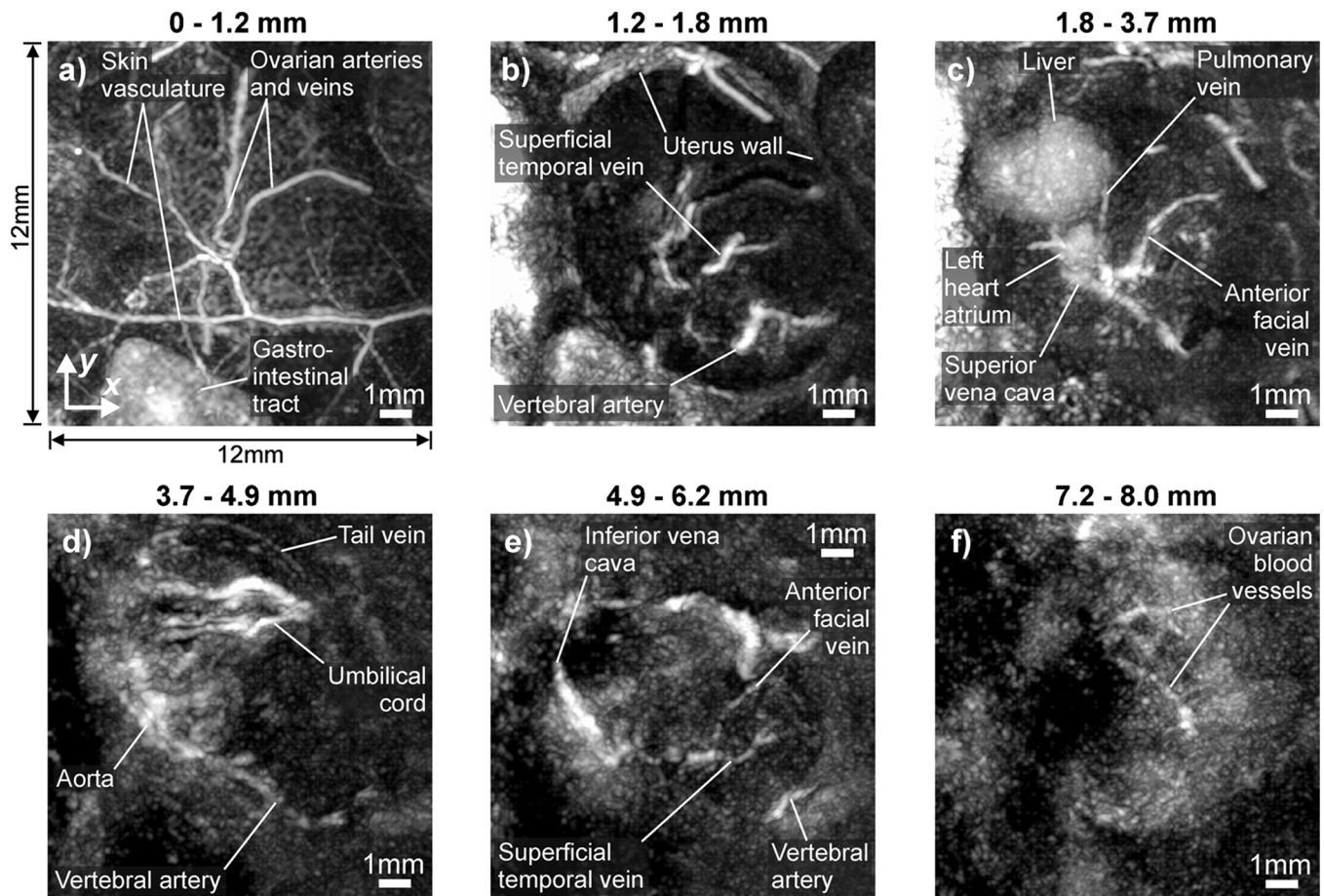


**Fig. 7** Subsections of the *in vivo* image data shown in Fig. 6 for different depth ranges. (a)  $x - y$  MIP for  $z = 0$  to 1.2 mm, which shows the vasculature in the skin and the uterus. (b)  $x - y$  MIP for  $z = 1.2$  to 1.8 mm, which shows some of the superficial vasculature of the embryo as well as the walls of the uterus. (c)  $x - y$  MIP for  $z = 1.8$  to 3.7 mm, which shows the left heart atrium, a variety of blood vessels, such as the pulmonary and anterior facial vein, as well as organs, such as the liver. (d)  $x - y$  MIP for  $z = 3.7$  to 4.9 mm, which shows major internal blood vessels, such as the aorta and the vertebral artery, and the umbilical cord. (e)  $x - y$  MIP for  $z = 4.9$  to 6.2 mm, which shows major internal blood vessels, such as the inferior vena cava, and external vessels, such as the superficial temporal vein. (f)  $x - y$  MIP for  $z = 7.2$  to 8.0 mm in which ovarian blood vessels can be discerned. A flythrough movie of the 3-D data set is available online (Video 6, MOV, 9.12 MB). [URL: <http://dx.doi.org/10.1117/1.JBO.17.6.061220.6>].

For example, Fig. 7(d) shows the aorta and vertebral artery, the tail vein and the umbilical cord. In Fig. 7(e) and 7(f), which show the MIPs for  $z = 4.9$  to 8.0 mm, major blood vessels, such as the inferior vena cava, the superficial temporal vein, and the vertebral artery are visible. External blood vessels on the side of the embryo furthest from the abdominal skin, such as the anterior facial vein, are also evident. This shows that sufficient penetration depth for *in vivo* imaging of whole mouse embryos *in utero* can be achieved. Figure 7(f) shows the structures characteristic of the uterine vasculature underlying the embryo at depths greater than 7.2 mm. The features in Figs. 6 and 7 are best observed in the flythrough movie of this data set (available in Video 6). This movie also clearly demonstrates that vascular features at a depth of up to 10 mm can be observed.

#### 4 Discussion and Conclusions

This study has shown that photoacoustic imaging can visualize the vascular anatomy of whole mouse embryos in the intact mother animal *in utero* and wholly non-invasively to depths of 10 mm. The ability to visualize both the embryonic and maternal vascular anatomy with high spatial fidelity is a consequence of several specific features of the instrumentation and

image reconstruction algorithm used in this study. First, the FP sensor provides acoustically small element sizes at MHz frequencies with significantly higher sensitivity than equivalently broad-banded piezoelectric detectors of the same size<sup>18</sup>—an essential prerequisite for achieving high image SNR and spatial resolution in the tomography mode of photoacoustic imaging. In addition, the time-reversal image reconstruction algorithm compensates for the acoustic band-limiting due to tissue acoustic attenuation yielding higher spatial resolution and contrast than non-compensated methods usually used in PA imaging. A further advantage, albeit one that relates more to convenience than performance, is derived from the transparent nature of the Fabry-Perot sensor head. Unlike most piezoelectric based photoacoustic scanners, this permits true backward mode operation which allows straightforward delivery of the excitation light and convenient interfacing of the instrument to the animal. The combination of these advantageous factors enabled *in vivo* visualization of intricate details of the embryonic vascular system. These include the vascular compartments of major organs, such as the heart ventricles, and major blood vessels, such as the aorta, the inferior vena cava, pulmonary vein, and the superficial temporal vein. The best images in terms of fidelity and quality were obtained in the *ex vivo* and *in situ* experiments, which

visualized the internal vasculature of major organs in greater detail than the *in vivo* images. Better *in vivo* imaging performance may be achieved by employing gating techniques similar to those used in MRI<sup>7</sup> to compensate for detrimental factors such as motion artefacts due to, for example, breathing, the beating of the heart, and possibly movements of the gastrointestinal tract.

The ability to obtain high resolution 3-D images of the vasculature of mouse embryos *in vivo* makes this technology applicable to, for example, longitudinal imaging studies of transgenic mouse embryos in which specific genetic knockouts induce heart and vascular malformations. These studies are currently carried out *ex vivo* using modalities such as MRI<sup>26</sup> or optical projection tomography,<sup>27</sup> which require extensive preparation of the excised embryos and may involve the draining of blood and the use of contrast agents, such as gadolinium or fluorescent dyes. By contrast, photoacoustic imaging has the potential to enable these studies to be conducted *in vivo*, over a period of time, and in a non-invasive manner thus making it a potentially powerful tool for developmental biological research.

### Acknowledgments

We would like to acknowledge the support of the British Heart Foundation and the Engineering and Physical Sciences Research Council.

### References

1. F. S. Collins, J. Rossant, and W. Wurst, "A mouse for all reasons," *Cell* **128**(1), 9–13 (2007).
2. M. H. Kaufman, *The Atlas of Mouse Development*, Vol. **512**, Academic Press, San Diego, CA (1992).
3. F. S. Foster, J. Hossack, and S. L. Adamson, "Micro-ultrasound for preclinical imaging," *Interface Focus* **1**(4), 576–601 (2011).
4. J. O. Cleary et al., "Cardiac phenotyping in *ex vivo* murine embryos using microMRI," *NMR Biomed.* **22**(8), 857–866 (2009).
5. J. O. Cleary et al., "Magnetic resonance virtual histology for embryos: 3D atlases for automated high-throughput phenotyping," *NeuroImage* **54**(2), 769–778 (2011).
6. J. T. Johnson et al., "Virtual histology of transgenic mouse embryos for high-throughput phenotyping," *PLoS Genetics* **2**(4), e61 (2006).
7. B. J. Nieman, K. U. Szulc, and D. H. Turnbull, "Three-dimensional, *in vivo* MRI with self-gating and image coregistration in the mouse," *Magn. Reson. Med.* **61**(5), 1148–1157 (2009).
8. C. A. Berrios-Otero et al., "Three-dimensional micro-MRI analysis of cerebral artery development in mouse embryos," *Magn. Reson. Med.* **62**(6), 1431–1439 (2009).
9. P. Beard, "Biomedical photoacoustic imaging," *Interface Focus* **1**(4), 602–631 (2011).
10. J. Laufer et al., "Quantitative spatially resolved measurement of tissue chromophore concentrations using photoacoustic spectroscopy: application to the measurement of blood oxygenation and haemoglobin concentration," *Phys. Med. Biol.* **52**, 141–168 (2007).
11. J. Yao et al., "In vivo photoacoustic imaging of transverse blood flow by using Doppler broadening of bandwidth," *Opt. Lett.* **35**(9), 1419–1421 (2010).
12. A. Sheinfeld, S. Gilead, and A. Eyal, "Simultaneous spatial and spectral mapping of flow using photoacoustic Doppler measurement," *J. Biomed. Opt.* **15**(6), 066010 (2010).
13. J. Brunker and P. Beard, "Pulsed photoacoustic Doppler flow measurements in blood-mimicking phantoms," *Proc. SPIE* **7899**, 78991K (2011).
14. J. Laufer et al., "Three-dimensional noninvasive imaging of the vasculature in the mouse brain using a high resolution photoacoustic scanner," *Appl. Opt.* **48**(10), D299–306 (2009).
15. E. Z. Zhang et al., "In vivo high-resolution 3D photoacoustic imaging of superficial vascular anatomy," *Phys. Med. Biol.* **54**(4), 1035–1046 (2009).
16. J. G. Laufer et al., "Photoacoustic imaging of vascular networks in transgenic mice," *Proc. SPIE* **7564**, 75641A (2010).
17. J. Xia et al., "Three-dimensional photoacoustic tomography based on the focal-line concept," *J. Biomed. Opt.* **16**(9), 090505 (2011).
18. E. Zhang, J. Laufer, and P. Beard, "Backward-mode multiwavelength photoacoustic scanner using a planar Fabry-Perot polymer film ultrasound sensor for high-resolution three-dimensional imaging of biological tissues," *Appl. Opt.* **47**(4), 561–577 (2008).
19. British Standard: Safety of laser products BS EN 60825-1:1994.
20. B. E. Treeby, E. Z. Zhang, and B. T. Cox, "Photoacoustic tomography in absorbing acoustic media using time reversal," *Inverse Problems* **26**(11), 115003 (2010).
21. B. E. Treeby and B. T. Cox, "k-Wave: MATLAB toolbox for the simulation and reconstruction of photoacoustic wave fields," *J. Biomed. Opt.* **15**(2), 021314 (2010).
22. T. L. Szabo, *Diagnostic Ultrasound Imaging*, Elsevier Academic Press, London (2004).
23. B. E. Treeby et al., "Automatic sound speed selection in photoacoustic image reconstruction using an autofocus approach," *J. Biomed. Opt.* **16**(9), 090501 (2011).
24. K. P. Köstli et al., "Temporal backward projection of photoacoustic pressure transients using fourier transform methods," *Phys. Med. Biol.* **46**, 1863–1872 (2001).
25. A. T. Soufan et al., "Three-dimensional reconstruction of gene expression patterns during cardiac development," *Physiol. Genom.* **13**, 187–195 (2003).
26. J. O. Cleary et al., "Cardiac phenotyping in *ex vivo* murine embryos using microMRI," *NMR Biomed.* **22**, 857–866 (2009).
27. J. R. Walls et al., "Three-dimensional analysis of vascular development in the mouse embryo," *PLoS One* **3**(8), e2853 (2008).